

Measurement Errors in Range-Based Localization Algorithms for UAVs: Analysis and Experimentation

Francesco Betti Sorbelli, *Member, IEEE*; Cristina M. Pinotti, *Member, IEEE*;
Simone Silvestri, *Senior Member, IEEE*; and Sajal K. Das, *Fellow, IEEE*

Abstract—Localizing ground devices (GDs) is an important requirement for a wide variety of applications, such as infrastructure monitoring, precision agriculture, search and rescue operations, to name a few. To this end, unmanned aerial vehicles (UAVs) or drones offer a promising technology due to their flexibility. However, the distance measurements performed using a drone, an integral part of a localization procedure, incur several errors that affect the localization accuracy. In this paper, we provide analytical expressions for the impact of different kinds of measurement errors on the ground distance between the UAV and GDs. We review three range-based and three range-free localization algorithms, identify their source of errors, and analytically derive the error bounds resulting from aggregating multiple inaccurate measurements. We then extend the range-free algorithms for improved accuracy. We validate our theoretical analysis and compare the observed localization error of the algorithms after collecting data from a testbed using ten GDs and one drone, equipped with ultra wide band (UWB) antennas and operating in an open field. Results show that our analysis closely matches with experimental localization errors. Moreover, compared to their original counterparts, the extended range-free algorithms significantly improve the accuracy.

Index Terms—Drone, localization algorithm, range-based, ground error, trilateration error, localization error



1 INTRODUCTION

In recent years, unmanned aerial vehicles (UAVs) or drones have received increasing attention from both the research and industry community. Of particular interest are applications enabled by combining UAVs with the Internet of Things (IoT) [1], [2], such as environmental monitoring [3], structural health monitoring [4], precision agriculture [5], search and rescue operations [6], and so on.

An important requirement of such applications is the ability to accurately localize the position of ground devices (GDs), making the collected data more meaningful. Since it is costly to equip each GD in the network with a GPS module, a fixed set of *anchor* devices, whose positions are known a-priori, is generally used [7]. Moreover, given the anchors use wireless transmissions to localize other GDs and their range is often limited, the number of required anchors could dramatically increase with the size of the network, thus increasing the cost of the localization procedure. This problem can be solved by replacing fixed anchor devices with a single *mobile anchor* (MA) equipped with a

GPS unit and periodically broadcasting its position to help nearby GDs localize.

Although there exists some work in the literature on localization based on ground MAs, such as rovers [8], relatively less has been proposed using flying MAs, like UAVs or drones [9], which is the focus of this paper. Compared to the ground MAs, the flying MAs are able to reach remote locations, move at a faster speed, and cover a wider area than terrestrial rovers [10]. Due to these advantages, in this paper we concentrate on localization algorithms involving flying MAs. When using UAVs as MAs, the distance can be estimated wirelessly by measuring the time of flight (ToF) between the MA and GDs. For distance measurements, in this paper we adopt the ultra wide band (UWB) technology [11].

Localization algorithms can be broadly categorized as *range-free* and *range-based* approaches [8]. In the range-free algorithms, the position is estimated without any type of measurements, but by only discovering if the GD and MA are in range. Among these, the *radius-based* approaches assume the knowledge of transmission radius [12], while the *radius-free* ones do not [13]. Such algorithms are often based on the assumption that the antenna radiation pattern is isotropic, which is unrealistic in general. In fact, our recent works [14], [15] have shown that the localization accuracy depends on the quality (pattern and radius) of the antenna, and how much they differ from the assumed isotropic pattern. On the other hand, in the range-based localization algorithms, the position of the GD is estimated by taking several measurements between it and the MA. These algorithms are known to be more accurate than range-free algorithms but at the cost of additional specialized

- Francesco Betti Sorbelli is with the Department of Computer Science, Missouri University of Science and Technology, Rolla, MO 65409, USA. Part of this work was done while F. Betti Sorbelli was working for the NALP-SAPR Project in Perugia.
- Cristina M. Pinotti is with the Department of Computer Science and Mathematics, University of Perugia, Italy.
- Simone Silvestri is with the Department of Computer Science, University of Kentucky, Lexington, KY 40506, USA.
- Sajal K. Das is with the Department of Computer Science, Missouri University of Science and Technology, Rolla, MO 65409, USA. Part of this work was done while S. K. Das was Satish Dhawan Visiting Chair Professor at the Indian Institute of Science, Bangalore - 560012, India.

hardware. For example, the estimation of distance exploits techniques like the received signal strength indicator (RSSI), the time of arrival (ToA), or the time difference of arrival (TDoA) [16].

Now, in any range-based localization procedure, *measurement errors* are unavoidable, and can seriously impact the localization accuracy. This is particularly relevant when the MA is a drone because the measurement errors can occur while calculating the distance between the MA and the GD. The magnitude of such errors depends on the adopted technology and on the quality of the air-to-ground (A2G) link between the MA and the GD. For example, the distance measurement error in a fully line of sight (LoS) link using the Wi-Fi technology is about 7–10 m; using Bluetooth it can be up to 15 m while it is only 10 cm using the UWB technology [17]. Additional errors may be caused by non-optimal weather conditions or the drone’s GPS *accuracy* [18]. For instance, the 3DR Solo drone used in our experiments has a GPS accuracy of 1 m [19]. In general, these errors propagate when combined and projected to the ground to localize the GDs. The error propagation depends on the specific localization technique, such as trilateration [20], intersection of points, centroid [21], [22], and so on.

Our Contributions: In this paper, we first provide bounds on various errors (e.g., instrumental error, rolling error, altitude error) impacting the estimated ground distance between the MA and GD. Then we focus on the commonly used *trilateration* based localization, and derive bounds on the propagation of ground distance errors on the estimated position of the GD. Finally, we perform extensive *in-field* experiments to quantify the localization accuracy of several existing state-of-the-art localization algorithms. Specifically, we consider the DRB-C [14] range-based algorithm, the DRF [23], IOC [13], and IOA [24] range-free algorithms extended to distance measurements, and two trilateration based algorithms like SCAN [25] and OMNI [26]. Our testbed uses two UWB DecaWave kits, namely EVK1000 kit [17] and MDEK1001 kit [27], and a 3DR Solo drone as the MA.

To the best of our knowledge, ours is the *first work* that provides an extensive in-field evaluation on the localization accuracy of the most relevant algorithms in the literature in real experimental settings using drones. Our novel contributions are summarized as follows.

- We derive bounds on various measurement errors (instrumental, rolling, and altitude) to estimate the impact on the estimated ground distance between the UAV (MA) and GD.
- We validate our theoretical analysis on the ground error with a simple set of static experiments using two UWB antennas. We observe the impact of measurement errors on the trilateration technique.
- Through experiments, we comprehensively compare three range-based and three range-free state-of-the-art localization algorithms using a UAV as MA, extending the range-free algorithms with distance measurements to significantly improve their localization accuracy. We also implement these algorithms employing 3DR Solo drone and ten GDs, the first such realistic testbed built.

The rest of the paper is organized as follows. Section 2 reviews the existing literature on localization approaches

relevant to our context. Section 3 derives expressions to approximate the measurement and ground errors, and introduces how our results are interpreted in the light of A2G communications. Section 4 investigates the localization error affecting the estimated position of the GD when the trilateration procedure is applied, and describes two localization algorithms based on trilateration compared in Section 6. Section 5 introduces four more localization algorithms not based on trilateration which are also compared using the testbed. Three of them are transformed from range-free to range-based algorithms. Section 6 presents a rich set of real experiments on the field aiming to evaluate the localization error of the different localization algorithms. Finally, Section 7 offers conclusions with directions of future research.

2 RELATED WORKS

This section reviews the relevant literature on localization of GDs using MAs and also efforts on testbed implementations considering UAVs as MAs.

2.1 MA-based Localization Algorithms

There exist many algorithms for ground MAs that can be classified as range-free and range-based. In the range-free localization algorithms, such as IOC [13] (intersection of circles) and IOA [24] (intersection of annuli), a rover broadcasts its current position at regular time intervals while following a path. From the heard and not-heard rover’s positions (informally, HnH technique), the GD builds a limited area where it may reside and places itself at the “center”. (More details about these algorithms are in Section 5.)

Usually range-free algorithms have relatively low localization accuracy, leading to the development of range-based algorithms as like SCAN and DOUBLE-SCAN [26]. In SCAN and DOUBLE-SCAN, the MA follows a path formed by vertical straight lines interconnected by horizontal lines. However, such algorithms result in a large number of collinear anchor points. Collinearity can be reduced by increasing the changes of direction in the path, as in HILBERT [26] and LMAT [28]. The path generated by LMAT logically tessellates the deployment area by equilateral triangles so that each GD falls inside a triangle. The vertices of the triangle where the GD resides are used to trilaterate the GD position, thus completely solving the collinearity issue. The above algorithms are designed for ground MAs.

A few localization algorithms have been proposed for flying MAs. Since the drone flies at a certain altitude, there are new constraints on the anchor points. In [29], one can find simulation comparisons of the above algorithms extended to flying MAs, with particular attention to the path length. The OMNI [25] algorithm is the first localization algorithm for drones that selects the anchor points in such a way that a certain accuracy is guaranteed. A simple and lightweight range-based algorithm called DRB-C [14] localizes the GDs by determining the correct intersection point of two circles exploiting a third reference point for the disambiguation. Finally, the DRF [23] algorithm, the first range-free algorithm for UAVs as MAs, exploits lightweight geometrical rules for position estimation. (See Section 5 for more details on OMNI and DRF.)

Very recently, in [30], a novel framework based on reinforcement learning (RL) has been proposed to enable a UAV

to autonomously find a suitable trajectory. This improves the localization accuracy of multiple GDs minimizing the flight time, path length, and UAV's energy consumption. As usual for RL techniques, an initial step is required for allowing the UAV to be trained for an online real scenario. However, this work does not mention how long this training phase lasts.

2.2 UAV based Testbeds for Localization Experiments

Recently, we performed preliminary experiments evaluating the range-free, radius-free DRF [23] algorithm using a UAV as MA and relatively inexpensive antennas [14]. Our conclusion was that the performance of DRF heavily depends on the shape of the antenna radiation pattern; precisely, the more the omnidirectionality of the antenna, the higher is the localization accuracy. Employing the DecaWave MDEK1001 kit, in [15], it has been experimentally shown that other range-free radius-based algorithms like IOC [13] and IOA [24], also exhibit higher accuracy with the omnidirectionality of antennas.

A real outdoor implementation of a range-based localization algorithm is presented in [31], which aims to localize a radio-frequency identification (RFID) ground tag with the help of a UAV. Initially, the RFID tag is detected by the UAV using its RFID reader. Then, the UAV takes hundreds of RSSI measurements and estimates the tag's position using a multilateration procedure. Experimental results show an average localization error of 6m. Note that this algorithm considers only random paths and random measurements, and does not investigate the relationship between the localization error and the UAV's altitude.

A range-based algorithm is experimentally tested in [32], in which a UAV regularly broadcasts its current GPS position while flying. The GD aims to detect a set of at least three equidistant RSSI distance measurements from its center in order to apply trilateration. Experimental results show an average error of 4m under normal conditions that reduces to 1m using GPS corrections provided by a Real Time Kinematic (RTK) algorithm. However, an RTK positioning system is not always available.

In [33] a testbed deploying five UWB ground anchors is implemented for evaluating and tracking the 3D position of a UAV equipped with UWB antenna. The anchors and the UAV are also equipped with GPS receivers with RTK capabilities. The experimental error between UWB and RTK distance measurements ranges from 2–24 cm, while the GPS positioning error alone is 2 m on an average. Another similar set-up employing UWB technology is proposed in [34] to localize a moving UAV. In this scenario, four fixed UWB anchor devices are placed on the ground. Experimental results show an average localization error of 1 m. Notice that, differently from the setting considered in this paper, the last two approaches [33], [34] aim at localizing or tracking the UAV (MA) instead of the GDs. Nonetheless, they employ UWB and UAV technologies.

3 MEASUREMENTS AND GROUND ERRORS

In this section, we provide analytical bounds on the impact of different measurement errors that may occur on the estimated ground distance between the MA and a GD.

3.1 Terminology and Notations

Let the *slant distance* s denote the 3D distance between the drone as MA and the GD. We define the *accuracy* as the maximum error in absolute value, and we let ϵ_s denote the *instrumental accuracy*, i.e., the maximum error in estimating the slant distance. Let the point P be the GD's position on the ground, the point \widetilde{W} be the actual drone's position, and the point W be the scheduled drone's position (see Figure 1).

The measured slant distance $s' = \widetilde{W}P$ can be different from the exact slant distance $s = WP$ due to the instrumental error and due to the accuracy of the drone's position (i.e., the drone resides at \widetilde{W} and not at the scheduled position W). Let the *slant error* E_s be the 3D measurement error that affects the measured slant distance s . The slant and the instrumental errors are depicted along with s in Figure 1.

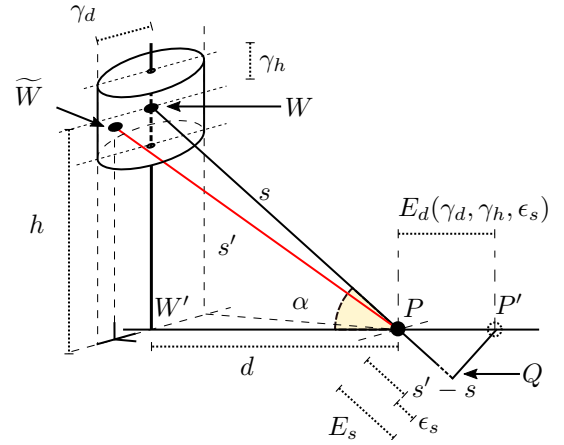


Fig. 1. The ground error: the point P is the GD.

In reality, the accuracy of the drone's position \widetilde{W} depends on its drift with respect to its trajectory, and on the changes of its altitude. Indeed, a drone is more unstable than a rover, even if it hovers in a given position. We say that the drone *rolls* when it drifts to some directions on a fixed plane, and that the drone *uplifts* or *downfalls* when it elevates or decreases its altitude, respectively. We denote with γ_d and γ_h , respectively, the *rolling* and the *altitude accuracy* that depend on the GPS, and the barometer. Figure 1 depicts the cylinder where the drones may reside due to the rolling and altitude errors. Interestingly, the drone resides inside a cylinder instead of a sphere since we consider γ_d and γ_h independently to each other. Let α in Figure 1 be the elevation angle as when there are no errors. That is, α is given assuming the scheduled position of the drone.

To localize the GD, we must convert the 3D slant distance s into the *ground distance* d , which is a distance derived on the 2D plane. The exact ground distance d is the distance $\widetilde{W}P$ between P and the projection W' on the ground of the drone's position W . That is, d assumes the drone to be in the scheduled position W . However, we do not know s , but we know s' . Then, let the *ground error* E_d be the measurement error $\widetilde{W}P'$, where P' is the position of P estimated on the ground by using the measured slant distance s' and the scheduled elevation angle α which assumes the exact ground distance d and the scheduled altitude h . Finally, let the *ground accuracy* ϵ_d be the maximum E_d .

TABLE 1
Summary of Notations for errors and accuracies.

symbol	description
α	elevation angle
ϵ_s	instrumental accuracy
γ_d	rolling accuracy
γ_h	altitude accuracy
ϵ_d	ground accuracy (max error)
E_d	ground error
E_s	slant error
E_L	localization error
E_L^T	localization trilateration error
ϵ_L^T	localization trilateration accuracy (max error)

The ground error E_d is the 3D slant error E_s as it is perceived on the ground. With a single measurement, we only know the relative distance between the MA and the GD, thus the GD is not yet localized. Beyond the ground error, there is the *localization error* E_L , which is instead the distance from the GD's estimated position (by any localization algorithm) and the GD's actual position. This error also depends on the invoked algorithm and its implicit rules to find the GD's position, and will be investigated farther.

Table 1 summarizes the notations used in this paper.

3.2 The Ground Error

In this section, we analytically study the ground error E_d by breaking it up into three independent components $E_d(\epsilon_s)$, $E_d(\gamma_d)$, and $E_d(\gamma_h)$ that, respectively, depend on: 1) the *instrumental accuracy*, 2) the *rolling accuracy*, and 3) the *altitude accuracy*. We recall that we define *accuracy* as the maximum error in absolute value. $E_d(\gamma_d)$ and $E_d(\gamma_h)$ model the error in the drone's position. Note that each component depends on an independent hardware part, namely, UWB, GPS, and barometer, and thus it makes sense to study them separately. Whenever we study one component, we assume the other errors to be null.

3.2.1 Instrumental error

Let us investigate $E_d(\epsilon_s)$, i.e., the impact of the *instrumental error* e_s on E_d . Note that e_s is defined as the difference, positive (overestimation) or negative (underestimation), between the measured distance and the actual distance. Moreover, ϵ_s is the absolute value of the maximum instrumental error. Accordingly, $|e_s| \leq \epsilon_s$. Here we assume $\gamma_d = \gamma_h = 0$. Let s be the exact 3D distance between the drone and the object P (P denotes the GD's position). Then, let $s' = s + e_s$ be the measure of the segment \overline{WP} , where $-\epsilon_s \leq e_s \leq \epsilon_s$. In the following, we geometrically show how the measured slant distance s' is converted into the ground distance. Figure 2 illustrates the reasoning behind the choice of $e_s = \pm\epsilon_s$. We draw a circumference of radius s' centered at the waypoint W . Such circumference will intersect the line that passes between W and P in Q (see Figure 2). Since the measured slant distance is different from the exact one, i.e., $s' \neq s$, Q does not coincide with P , and Q is not at the ground level. Specifically, the segment \overline{PQ} of length $e_s = s' - s$ is on the extension of \overline{WP} if $e_s > 0$; whereas \overline{PQ} is on the radius \overline{WP} if $e_s < 0$.

Since in general $\epsilon_s \ll s$, we can approximate the circumference of radius s' with its tangent in Q . The point P' ,

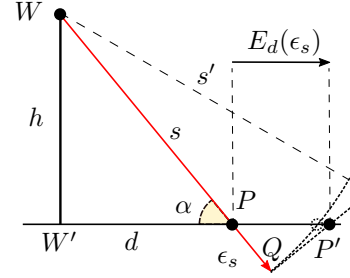


Fig. 2. Overestimation in the instrumental accuracy ϵ_s .

where the tangent intersects the ground¹, is the estimated position for P according to the measurement s' . Thus, recalling that W' is the projection of W on the ground, $\overline{PP'}$ is the error on the ground derived from the slant error e_s . By elementary geometric rules applied to the right-angled triangle PQP' , we obtain $\overline{PP'} = e_s \cdot \frac{1}{\cos(\alpha)} = e_s \cdot \sqrt{1 + \frac{h^2}{d^2}}$, where h is the drone's altitude. because $\angle QPP'$ is equal to the elevation angle α . The error $E_d(\epsilon_s)$, when the instrumental error is maximum and the object is at ground distance d from the drone, is given by:

$$E_d(\epsilon_s) = \epsilon_s \cdot \frac{1}{\cos(\alpha)} = \epsilon_s \cdot \sqrt{1 + \frac{h^2}{d^2}}. \quad (1)$$

The ground error $E_d(\epsilon_s)$ varies with the distance d on the ground. When $h \neq 0$, the error increases when d decreases (whereas, when $h = 0$ the error does not depend on d). When $h \neq 0$, the worst case occurs when the drone is perpendicular to the point to be measured (i.e., $W' = P$, $d = 0$, $E_d \rightarrow \infty$). From this observation, we can assert that, when the measurements are taken by a UAV, rather than a rover, in order to bound $E_d(\epsilon_s)$, it is convenient to add the constraint that all the measurements have to respect a given *minimum ground distance* d_{\min} .

3.2.2 Rolling error

In this section, we only consider the rolling error (i.e., $\epsilon_s = \gamma_h = 0$). When the drone hovers in position $W = (x, y, z)$, it may not be in W , but rather in position \tilde{W} due to the GPS accuracy or the bad weather conditions (see Figure 3).

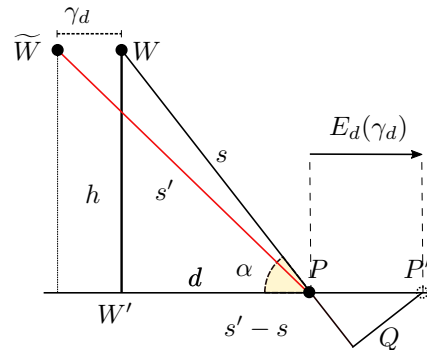


Fig. 3. The rolling accuracy $\gamma_d > 0$ and ground error.

To better define the rolling error, we set a 3D-Cartesian coordinate system whose origin is the projection $W' =$

1. Figure 2 shows the intersection P' between the tangent and the ground, which approximates the intersection (white dot) between the circumference and the ground. However, the two intersections become closer and closer when s increases.

$(0, 0, 0)$ on the ground of the exact drone's position W , whose x -axis passes through the object to measure P , and z -axis passes through W . Thus, $W = (0, 0, h)$ and $P = (d, 0, 0)$. Then, let the actual drone's position be $\widetilde{W} = (e_x, e_y, h)$, with $-\gamma_d \leq e_x, e_y \leq \gamma_d$, where γ_d is the rolling accuracy. Obviously, $\widetilde{W}' = (e_x, e_y, 0)$ is the projection of \widetilde{W} on the ground, which is inside a circle of radius γ_d centered at the origin W' . For each point of the circle, it holds $e_x = \gamma_d \cos(\psi)$ and $e_y = \gamma_d \sin(\psi)$, where $\psi = \angle \widetilde{W}'W'P$ and $0 \leq \psi \leq 2\pi$. The measured slant distance s' between \widetilde{W} and P given by:

$$\begin{aligned} s' &= \sqrt{h^2 + (d - e_x)^2 + e_y^2} \\ &= \sqrt{h^2 + (d - \gamma_d \cos(\psi))^2 + (\gamma_d \sin(\psi))^2} \\ &= \sqrt{h^2 + d^2 - 2d\gamma_d \cos(\psi) + \gamma_d^2 \cos^2(\psi) + \gamma_d^2 \sin^2(\psi)} \\ &= \sqrt{h^2 + d^2 - 2d\gamma_d \cos(\psi) + \gamma_d^2} \end{aligned}$$

Recalling that $h > 0, d > 0, \gamma_d \geq 0$ and $0 \leq \psi \leq 2\pi$, we note that s' is maximum when $f = -2d\gamma_d \cos(\psi)$ is minimum.

Including the instrumental error, the slant error is:

$$E_s = s' - s = \sqrt{h^2 + d^2 - 2d\gamma_d \cos(\psi) + \gamma_d^2} - \sqrt{h^2 + d^2}$$

which is maximum when $\cos(\psi) = -1$ and $\epsilon_s > 0$.

In order to project E_s on the ground, we repeat the same construction as in Section 3.2.1. We draw a circumference of radius s' centered in the waypoint W , which intersects the line that passes for W and P in Q . The tangent in Q intersects the ground in the estimated position P' . Applying elementary trigonometry to the right-angled triangle PQP' whose $\angle QPP'$ is equal to the elevation angle α ,

$$\begin{aligned} E_d(\gamma_d) &= \frac{E_s(\gamma_d)}{\cos(\alpha)} = \frac{|s' - s|}{\cos(\alpha)} = \frac{|(s')^2 - (s)^2|}{\cos(\alpha)(s' + s)} \\ &= \frac{|\gamma_d^2 - 2d\gamma_d \cos(\psi)|\sqrt{h^2 + d^2}}{(s' + s)d} = \frac{|\gamma_d^2 - 2d\gamma_d \cos(\psi)|s}{(s' + s)d} \end{aligned}$$

When $s' > s$ (i.e., $\frac{\pi}{2} < \psi < \frac{3\pi}{2}$), that is, when the drone rolls away from the object, it holds:

$$E_d(\gamma_d) \leq \frac{|\gamma_d^2 - 2d\gamma_d|}{2d}$$

and assuming $\gamma_d \ll d$

$$E_d(\gamma_d) \leq \gamma_d \quad (2)$$

When $s' < s$ (i.e., $0 \leq \psi \leq \frac{\pi}{2}$ or $\frac{3\pi}{2} \leq \psi \leq 2\pi$), that is, when the drone rolls close to the object, since $s + s' > s$, we obtain a weaker bound:

$$\begin{aligned} E_d(\gamma_d) &< \frac{|\gamma_d^2 - 2d\gamma_d|}{d} \frac{s}{s'} \\ &< 2\gamma_d \end{aligned}$$

Now, if $\gamma_d \ll d$ holds, $\frac{s}{s'} \rightarrow 1$. Since $s + s' \geq 2s'$, we have:

$$\begin{aligned} E_d(\gamma_d) &< \frac{|\gamma_d^2 - 2d\gamma_d|}{2d} \frac{s}{s'} \\ &< \gamma_d \frac{s}{s'} \rightarrow \gamma_d \quad (3) \end{aligned}$$

We will see in our experiments that indeed the stricter bound in Eq. (3) well approximates the rolling error even when the drone rolls close to the GD.

3.2.3 Altitude error

In this section, we only consider the altitude error (i.e., $\gamma_d = \epsilon_s = 0$). When the drone is subject to an uplift (resp., downfall), the measured slant distance s' is overestimated (resp., underestimated). The overestimate case is illustrated in Figure 4.

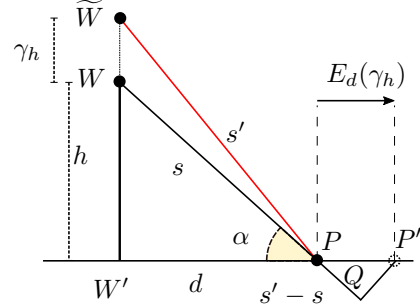


Fig. 4. The altitude accuracy $\gamma_h > 0$ and ground error.

The measured slant distance s' between \widetilde{W} and P is: $s' = \sqrt{h + \gamma_h^2 + d^2}$. Recalling that $h > 0, d > 0$, and $\gamma_h \geq 0$, including the instrumental error, the slant error is:

$$E_s = s' - s = \sqrt{h + \gamma_h^2 + d^2} - \sqrt{h^2 + d^2}$$

Moreover,

$$E_d(\gamma_h) = \frac{E_s(\gamma_h)}{\cos(\alpha)} = \frac{|s' - s|}{\cos(\alpha)} = \frac{|\gamma_h^2 - 2h\gamma_h|s}{(s' + s)d}$$

Repeating calculations similar to those above, and assuming that the altitude accuracy γ_h is very small with respect to h , and that $\frac{s}{s'} \rightarrow 1$, we find that the ground error can be approximated as:

$$E_d(\gamma_h) \approx \gamma_h \frac{h}{d} \quad (4)$$

3.2.4 Overall ground error

From the previous discussions we can estimate the overall ground error as stated by the following:

Fact 1. Let ϵ_s , γ_d , and γ_h be respectively the instrumental accuracy, rolling accuracy, and altitude accuracy that may affect the slant measurement. By projecting the slant distance on the ground, the largest error E_d given the ground distance d , is:

$$E_d(\gamma_d, \gamma_h, \epsilon_s) \approx \gamma_d + \frac{h}{d}\gamma_h + \epsilon_s \sqrt{1 + \frac{h^2}{d^2}} \quad (5)$$

Analyzing Eq. (5), it is clear that when d is very small, the ground error is very large. Increasing d , the impact of both instrumental and altitude accuracies decreases, but E_d cannot be smaller than the rolling accuracy γ_d .

In conclusion, the ground error can be bounded by adding a constraint on the minimum ground distance (d_{\min}) between the drone and the GD. If it is ensured that $d \geq d_{\min}$ using the drone, then the ground accuracy ϵ_d , i.e., the maximum error on the ground distance, is bounded by:

$$\epsilon_d = \epsilon_d(\gamma_d, \gamma_h, \epsilon_s) \approx \gamma_d + \frac{h}{d_{\min}}\gamma_h + \epsilon_s \sqrt{1 + \frac{h^2}{d_{\min}^2}} \quad (6)$$

Our first takeaway is that the ground accuracy ϵ_d can be monitored by monitoring the ratio h/d between altitude and ground distance.

A2G links and ground error: In this paragraph, we explain how the A2G communication link quality between GD and MA impacts on our results. According to the model in [35], each A2G link has a certain probability $P(\text{LoS})$ to be in LoS and $P(\text{NLoS})$ to be in NLoS. $P(\text{LoS})$ depends on the elevation angle α between drone and GD and on the environment type, i.e., sub-urban, urban, dense, and highrise. Clearly, in crowded environments, links have a higher probability to be mixed LoS and NLoS scenarios.

TABLE 2
The line of sight probabilities $P(\text{LoS})$ in different environments [35].

h/d_{\min}	α	sub-urban	urban	dense	highrise
5.67	80°	100%	100%	100%	100%
$\sqrt{3}$	60°	100%	100%	100%	60%
1	45°	100%	97%	85%	30%
1/2	26.5°	100%	75%	30%	5%
1/3	20°	100%	40%	20%	$\rightarrow 0\%$

The UWB distance measurements are possible as long as the antennas keep an A2G link. Up to 35 m, even if the elevation angle is small, communications can be established since UWB works in both LoS and NLoS [36]. Beyond 35 m UWB only works in LoS, and hence only LoS links can be guaranteed. Suitable values for h/d_{\min} such that the elevation angle $\alpha = \arctan(h/d_{\min})$ gives LoS links with high probability, have to be selected. For example, as reported in Table 2, in sub-urban environment $h/d_{\min} = 1/3$ because A2G link has 100% probability to be LoS whenever $\alpha \geq 20^\circ$. In urban environment, links are 100% in LoS when $h/d_{\min} \geq 1/2$ ($\alpha \geq 26.5^\circ$). Similarly, in highrise the minimum ratio for LoS links is $h/d_{\min} = 5.67$. Note that for $h/d_{\min} < 1/3$ ($\alpha < 20^\circ$) links could be mixed and hence UWB might work or not. Recall that the ground accuracy in Eq. (6) can be bounded selecting a small h/d_{\min} . Keeping in mind the maximum UWB NLoS range of 35 m, h/d_{\min} cannot be freely chosen. However, in our experiments since we work in a sub-urban, obstacle-free, and flat environment, any ratio $h/d_{\min} \geq 1/3$ is sufficient to be in LoS.

4 LOCALIZATION ERROR FOR TRILATERATION BASED ALGORITHMS

Once a GD has collected a suitable number of distance measurements from the MA, it can be localized by invoking any localization algorithm. A very common approach for localization is *trilateration*. In Section 4.1 we analytically derive the *localization trilateration error* E_L^T and the *localization trilateration accuracy* ϵ_L^T , which are incurred by any algorithm based on this method. Subsequently, in Section 4.2, we discuss the trilateration based algorithms that are considered in our experiments.

4.1 Trilateration Error

This section discusses the localization error E_L^T that may affect the estimated GD's position when the trilateration procedure is applied.

Let us briefly recall that the trilateration procedure for estimating the position of the object P , takes as input three ground distances d_1 , d_2 , and d_3 of P from three waypoints W_1 , W_2 , and W_3 respectively. The procedure returns, as the GD's estimated position P , the intersection of the three circumferences corresponding to the radii d_1 ,

d_2 , and d_3 centered at the projections W'_1 , W'_2 , and W'_3 of the waypoints. Due to the ground errors, however, the three circumferences do not intersect at a single point, but they delimit a small *star* area, as depicted in Figure 5a. In fact, a pair of extreme circumferences, one obtained by considering the radius affected by the maximum positive E_d error ($d_i + E_d$, measurement overestimation) and one whose radius is affected by the maximum negative E_d error ($d_i - E_d$, measurement underestimation) is drawn in place of each circumference of radius d_i .

Assuming that all the ground distances are sufficiently large compared to the ground error, these extreme circumferences can be linearized (i.e., replaced by the tangent to the radius) without significantly changing the area. Each different non-parallel pair of linearized circumferences intersects at a single point forming overall 12 different points, that correspond to the vertices of the star shape. Note that P is at the center of the star. The trilateration procedure returns as the estimated position, instead of the exact intersection P , a point P' in the star. The point P' is selected by means of the least-squares-error method. In fact, given three ground measurements, the estimated position of P is the point (x_P, y_P) that minimizes the sum of the least squares, i.e.:

$$\begin{aligned} \min \quad & \delta_1^2 + \delta_2^2 + \delta_3^2 \\ \text{s.t.} \quad & \sqrt{(x_{W'_i} - x_P)^2 + (y_{W'_i} - y_P)^2} + \delta_i = \overline{W'_i P} \quad (7) \\ & \text{for } i = 1, 2, 3. \end{aligned}$$

The largest value of the positioning error, i.e., $\overline{PP'}$, called *localization trilateration error* E_L^T , or simply *trilateration error*, occurs when the estimated position P' is at the furthest vertex of the star shape. In other words, the positioning error is bounded by the distance between the center of the star P (i.e., the actual position of the GD) and its furthest vertex.

As an example, in Figure 5b, the distance between the actual point P and the estimated point P' at the intersection of two measurement underestimations $d_2(-)$ and $d_3(-)$ is $\frac{E_d}{\cos(\beta/2)}$, where β is one of the three different angles in which the turn angle in P is divided by the lines $\overline{W'_1 P}$, $\overline{W'_2 P}$, and $\overline{W'_3 P}$ (see Figure 6a). In Figure 5c, the distance between P and P' that results from the measurement underestimation, i.e., $d_1(+)$, and the measurement overestimation, i.e., $d_3(-)$, is depicted. In this case, the distance $\overline{PP'} = \frac{E_d}{\sin(\beta/2)}$.

For each vertex of the star, depending on the signs of the estimations (+ overestimation, - underestimation) of each pair of circumferences, we have: $\frac{E_d}{\sin(\beta_i/2)}$ if the signs are the same; and $\frac{E_d}{\cos(\beta_i/2)}$ if the signs are different, where $\beta_1 \leq \beta_2 \leq \beta_3$ are the three different angles formed in P such that $\sum_i \beta_i = \pi$. In the following, we prove that the furthest vertex occurs when the measurement estimations have the same signs and the angle is minimum.

Lemma 1 ([37]). *Let $\beta_{\min} = \min_i\{\beta_i\}$, $\beta_{\max} = \max_i\{\beta_i\}$ and $\sum_i \beta_i = \pi$. Then $\sin(\frac{\beta_{\min}}{2}) \leq \cos(\frac{\beta_{\max}}{2})$.*

Proof: Let $\beta_{\min} = \min_i\{\beta_i\}$ and $\beta_{\max} = \max_i\{\beta_i\}$. Then, we have: $\beta_{\max} \leq \pi - 2\beta_{\min} \Rightarrow \frac{\beta_{\max}}{2} \leq \frac{\pi}{2} - \beta_{\min}$ from which $\cos(\frac{\pi}{2} - \beta_{\min}) \leq \cos(\frac{\beta_{\max}}{2})$, and thus $\sin(\beta_{\min}) \leq \cos(\frac{\beta_{\max}}{2})$. Since $0 \leq \beta_{\min} \leq \pi/3$, it yields:

$$\sin\left(\frac{\beta_{\min}}{2}\right) \leq \sin(\beta_{\min}) \leq \cos\left(\frac{\beta_{\max}}{2}\right)$$

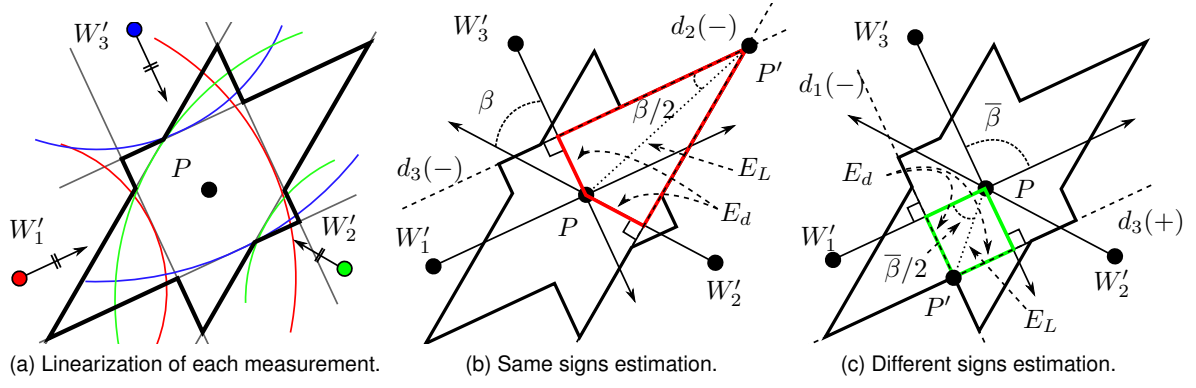


Fig. 5. Trilateration error with different conditions.

Thus, the furthest vertex is at distance $\frac{E_d}{\sin(\frac{\beta_{\min}}{2})}$ from P . \square

Theorem 1 ([37]). *Given the accuracies ϵ_s , γ_d , and γ_h , given d_{\min} , and recalling that $\epsilon_d(\gamma_d, \gamma_h, \epsilon_s) \approx |\gamma_d| + \frac{h}{d_{\min}}|\gamma_h| + |\epsilon_s|\sqrt{1 + \frac{h^2}{d_{\min}^2}}$, the localization trilateration accuracy defined as the maximum trilateration error is obtained as:*

$$\epsilon_L^T(\gamma_d, \gamma_h, \epsilon_s) = \frac{\epsilon_d(\gamma_d, \gamma_h, \epsilon_s)}{\sin\left(\frac{\beta_{\min}}{2}\right)} \quad (8)$$

Therefore, from Eq. (8), we learn that, given a certain ground error, the localization error is minimized when $\beta_{\min} \rightarrow \frac{\pi}{3} = 60^\circ$. Figure 6b reports an example of the trilateration error E_L^T computed by varying both the values d and β_{\min} , and assuming only the instrumental error, i.e., $\gamma_d = \gamma_h = 0$ m and $\epsilon_s = 0.10$ m. As expected, when both d and β_{\min} tend to 0, E_L^T grows quickly.

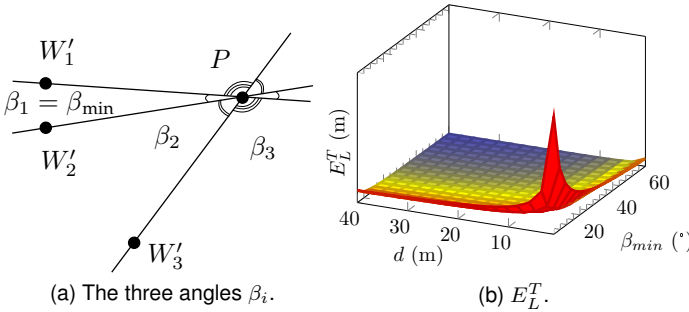


Fig. 6. The trilateration error E_L^T : when d and β_{\min} are very small, the error is extremely high.

Analyzing Eq. (8) it is clear that the localization trilateration accuracy ϵ_L^T can be bounded keeping the minimum angle β_{\min} as large as possible, i.e., closer to 60° .

Our second takeaway is that a good localization accuracy in trilateration methods can be obtained keeping as low as possible the ratio h/d_{\min} , the elevation angle α as small as possible respecting also the communication conditions in LoS, and making the minimum angle β_{\min} as large as 60° .

4.2 OMNI and SCAN Localization Algorithms

In this section, we review trilateration based algorithms OMNI and SCAN considered in our experiments. Based on the above discussion, the localization error for these algorithms is bounded by ϵ_L^T , which is a function of the

accuracies ϵ_s , γ_d , and γ_h , the minimum angle β_{\min} , altitude h , and minimum distance d_{\min} . Both algorithms are based on a static path Π formed by a series of vertical lines (each called as *vertical scan*) connected by horizontal lines.

The SCAN Algorithm: SCAN [26] is one of the first range-based localization algorithms designed for rovers. Each GD is localized employing trilateration using three waypoints. The main drawback is the collinearity between points in the estimation phase. Since we wish to avoid such undesirable conditions, in our experiments we perform single trilateration selecting three non-collinear waypoints from at least two distinct vertical scans. In this slightly improved version of SCAN, the β_{\min} and d_{\min} constraints may not be satisfied, resulting in large localization errors.

The OMNI Algorithm: OMNI [25] is the first range-based localization algorithm that takes into account the impact of the drone's altitude on the measurement accuracy and on the geometry of the waypoints from which trilateration is performed. It logically tessellates the deployment area into diamonds. Then, each GD, once it has acquired a sufficient number of waypoints/distances from the drone, performs two trilaterations. The first trilateration is invoked using any three non-collinear waypoints in order to compute the logical diamond in which the GD resides. Since each diamond is associated with an optimal triple of waypoints which satisfy the minimum angle/distance constraints [25], any GD belonging to such diamond can be finally trilaterated for a second time using that triple. In conclusion, OMNI has been proved to be highly accurate but requires two trilaterations, as opposed to the single trilateration performed by SCAN.

5 OTHER LOCALIZATION ALGORITHMS

In this section, we describe four more localization algorithms, namely DRF, IOA, IOC, and DRB-C, not based on trilateration. The first three of such algorithms are *range-free*, therefore the localization accuracy depends on the antenna radiation pattern quality. Recently, Betti et al. [14] experimentally showed the poor accuracy of DRF using relatively inexpensive hardware. In this paper, motivated by these results, we extend these algorithms by considering distance measurements to improve on the localization accuracy. Specifically, as also detailed in the experiments in Section 6, the GD stores, for each waypoint that it hears, the relative distance between itself and that waypoint. Exploiting this

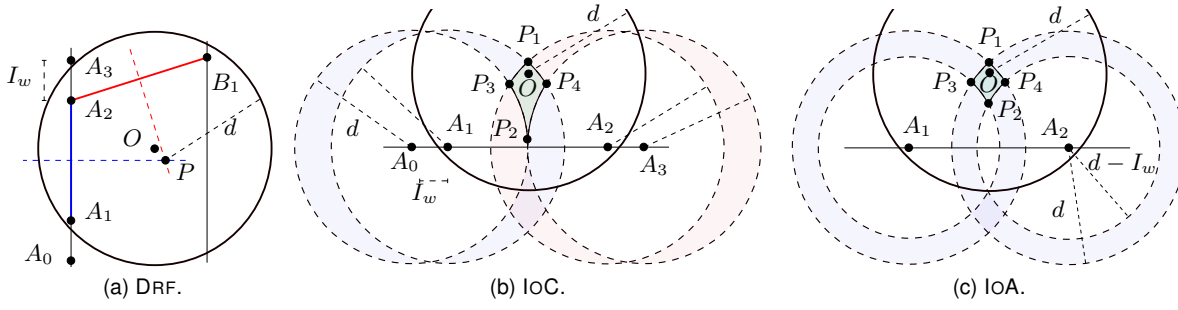


Fig. 7. The DRF, IoC, and IOA localization algorithms. In IoC e IOA there are two symmetric intersection areas: a third point is required to find and disambiguate the correct intersection area.

information, we reformulate all the range-free techniques making them actually range-based. This way, we mean to overcome the poor localization accuracy resulting from the low-quality of the radio antenna, while still keeping the original procedures for the localization.

In the following, for each of these extended algorithms, as well as for DRB-C, we identify the sources of the localization error. However, we do not derive any analytical expression of E_L , since the analysis would involve too many variables to be expressed in a closed formula. Nevertheless, we study their error through real experiments in Section 6.

The DRF Algorithm: DRF [23] is a lightweight range-free radius-free algorithm designed for drones. This algorithm is based on the notion of *chord*. In general, the perpendicular bisector of any chord passes through the center O of the circle itself. So, the bisector of another non-parallel chord and the previous one intersect at O point. In Figure 7a, two chords are identified by the pairs A_1A_2 and A_2B_1 . Theoretically, the circle is identified by the receiving disk of GD which is centered at O . Accordingly, the GD starts to estimate its position when it detects two chords. The two chords are detected using the HnH technique [15] on each scan. The detection of chords incurs several problems that eventually affects the localization accuracy. First, recalling that the MA regularly broadcasts its current position (waypoint) at discrete intervals of time and that two consecutive waypoints are at distance *inter-waypoint* I_w , the endpoints of the chords may not exactly fall on the circumference of the receiving disk, even if the receiving disk is a perfect circle (e.g., A_2 and A_3 in Figure 7a). However, the chords can be improperly defined if the antenna pattern has “holes” and “bubbles”, as experienced in the field as reported in [15].

Range-based extension: Exploiting the fact that our tested kit allows us to take distance measurements, the choice of the chords can be performed selecting three waypoints at a certain fixed distance d from the GD, relaxing the range-free constraint. In this way, with three waypoints on the same circumference of radius d , two chords can be derived. Accordingly, we can obtain a localization error which depends only on the length of I_w and on the error E_d . A more detailed explanation of the original version of DRF can be found in [14].

The IoC Algorithm: IoC [13] is a range-free radius-based localization algorithm initially developed for ground MAs. Like DRF, the IoC algorithm exploits the HnH method in order to detect special points used for building a constraint

area that bounds the GD’s position. However, diversely from DRF, IoC relies also on the value of the communication radius d . In fact, initially the GD detects the pair of endpoints (A_1 and A_2 , in Figure 7b) using the HnH method. Successively, two more points called pre-arrival and post-departure (A_0 and A_3), respectively, are determined using the value of I_w , since MA sends its current position at discrete intervals. Note that such four points belong on the same straight line. Then, four circles of radius d centered at each of these four points are drawn. Those circles create two symmetrical intersection areas where the GD may reside. In order to select the correct intersection area, the GD needs to detect a third point. Finally, the GD is localized at the “center” of the correct intersection area. This definition of center slightly varies depending on the shape of the intersection area, which may vary from four to five vertices.

Range-based extension: As for DRF, also in IoC we exploit the distance measurements for computing all the required points. That is, we select the two waypoints on the same line at distance d from GD as A_1 and A_2 , and the preceding and subsequent waypoints as A_0 and A_3 .

The IOA Algorithm: IOA [24], is a range-free radius-based algorithm very similar to IoC. Indeed, it builds a similar constrained area using the HnH method and the knowledge of both d and I_w . Once the GD has detected the two extreme endpoints (A_1 and A_2 , in Figure 7c), it traces two circles of radius d and $d - I_w$ on both the points. These circles, which create two annuli, intersect in two distinct and symmetrical intersection areas, so also in this case a third point is required. Finally, the GD estimates its position at the center of such an area, using easy geometrical rules.

Range-based extension: As for the previous algorithms, we select the two extreme endpoints A_1 and A_2 as two waypoints at distance d from the GD.

The DRB-C Algorithm: DRB-C [14] is a lightweight range-based technique designed for UAVs. The goal of GD is to detect two waypoints at distance d_1 and d_2 , and drawing two circumferences centered at these waypoints, of radius d_1 and d_2 , respectively. Then, the GD knows to reside simultaneously on the two intersections of two circumferences, and a third point is required to disambiguate the correct intersection point. In conclusion, we can note that, differently from the trilateration based algorithms OMNI and SCAN in which the least-squares-error method is employed (see Eq. (7)), DRB-C only demands a few algebraic calculations.

Finally, Table 3 summarizes the six algorithms that will be compared in our testbed.

TABLE 3
Summary of the compared algorithms.

name	method	points	error source
OMNI [25]	trilaterations	3 + 3	geometry
SCAN [26]	trilateration	3	geometry
DRB-C [14]	circles intersection	2 + 1	center
DRF [23]	bisector intersection	3	chords
IoC [13]	points "center"	2 + 1	center
IOA [24]	points "center"	2 + 1	center

6 EVALUATION ON A REAL TESTBED

In this section we propose our experimental evaluation. Initially, in Section 6.1 we describe the adopted hardware for our testbed. In Section 6.2, we study the ground error E_d . In Section 6.3, we study the localization error E_L^T of the trilateration method. Finally, in Section 6.4, we run a campaign of experiments with the goal of comparing the localization error of different algorithms.

6.1 Performance of UWB Antennas

The experiments in Sections 6.2 and 6.3 are done using the DecaWave EVK1000 kit (see Figure 8a), formed by two UWB antennas which are based on the DW1000 UWB chip [17]. For the experiments done in Section 6.4, we rely on a more consistent set of twelve antennas, using the MDEK1001 kit (see Figure 8b), based on the same DW1000 UWB chip [27].

According to DecaWave, those chips have a 6.5 GHz center frequency, and have a declared and reliable point-to-point range up to 60 m LoS and 35 m NLoS [27] on a typical use-case. Although the DW1000 chip transmitting power is set to -41.3 dBm/MHz, and the typical receiver sensitivity is -93 dBm/500MHz [17], the received power is influenced by the antenna polarity. In both the DecaWave kits the antennas are vertically polarized, meaning that the module is intended to be vertically positioned to let another vertically polarized antenna observe an omnidirectional radiation pattern in the azimuth plane [27]. For this reason, following the recommendations provided by DecaWave in their datasheet, in our experiments we always vertically placed our antennas. The antenna placed on the drone is positioned vertically, but reversely, keeping the transceiver on the bottom, for avoiding the MA's body to become an obstacle between the GDs and the MA itself.

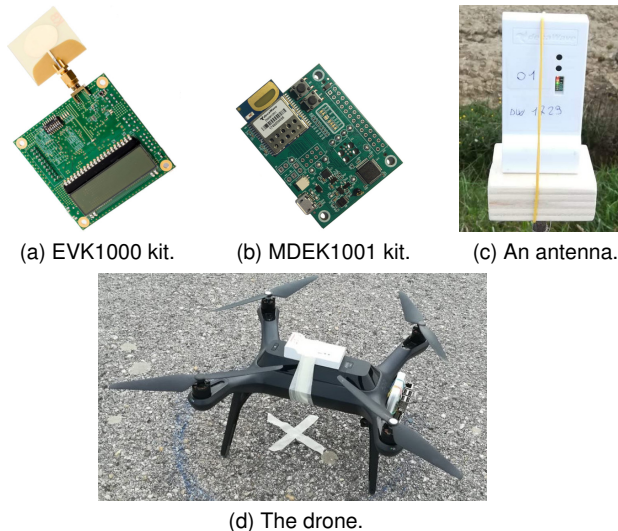


Fig. 8. The used DecaWave kits and the 3DR Solo drone.

6.2 Experiments with Ground Error

In this section we analyze the ground error employing the DecaWave EVK1000 kit. We start with pre-arranged antenna experiments in which two antennas (one reproduces the GD to localize and another one the MA) are used. The antenna that acts as GD is fixed on the ground, while the other one (MA), fixed on a pole, moves accordingly to the specific experiment emulating the rolling and altitude error. We fixed the drone's position on the ground and that of the GD measuring the distance with a Bosch digital laser [38]. The ground GPS drone's position is then converted as the origin $W' = (0, 0, 0)$ of the local Cartesian coordinate system used during the experiments. Then, in the subsequent experiments, we replace the pole with a drone hovering at a certain altitude. The goal is to understand how the drone impacts the measurement error. For each experiment, we record at least 30 slant distances and we finally determine the final computed value at the 95% confidence level.

In the first experiment, we measure the slant distance and comparing its projection on the ground with the exact ground distance d . Consequently, we compute the *experimental ground error* \overline{E}_d and compare it with theoretical error E_d . To verify Eq. (1), Eq. (2), and Eq. (4), we have measured and reported in Figure 9a, Figure 9b, and Figure 9c the experimental error \overline{E}_d when the instrumental error, rolling error, and altitude error, separately affect the GD on the ground, respectively. We also report the theoretical ground error bound E_d . It is interesting to see that, in each plot, the measurement error E_d (solid line) almost always upper-bounds the experimental error \overline{E}_d (dashed line). We also measured and reported in Figure 9d the combined error where all the three components affect the error along with the bound in Eq. (6). The curves almost coincide.

In the second experiment, we repeat the previous setting employing this time a drone. In Figure 9e we report the experimental \overline{E}_d for different altitudes. Since the drone's position is affected by the wind, air density, humidity, the strength of the propellers, and GPS error, we know that even the slant distance is affected at the same time. Moreover, we know from Eq. (6) that the error \overline{E}_d increases when h increases and when d tends to 0 m. In Figure 9e, we also plot the theoretical error E_d in solid lines, fixing $\epsilon_s = 0.10$ m and using $\gamma_d = \{0.6, 0.8, 1.2\}$ m and $\gamma_h = \{0.1, 0.15, 0.2\}$ m for each $h = \{10, 20, 30\}$ m, respectively, that empirically fit the experimental curves. Differently from the previous ones, this is the first experiment that somehow simulates a real scenario. It is interesting to note that, we can model the curve of the combined error even in a non-optimal scenario, just tuning in advance the parameters on Eq. (6), which provides a good approximation of the error.

In conclusion, upon this first campaign of experiments, we can confirm that the measurement error is small when either the ground distance between the drone and the GD is large or the altitude of the drone is low.

6.3 Experiments on the Trilateration Error

In this section, we describe two more comparative experiments to better understand how the localization error can be affected when the trilateration method is applied. From Eq. (8), it is clear that the localization error E_L can be bounded if the three waypoints are sufficiently apart from

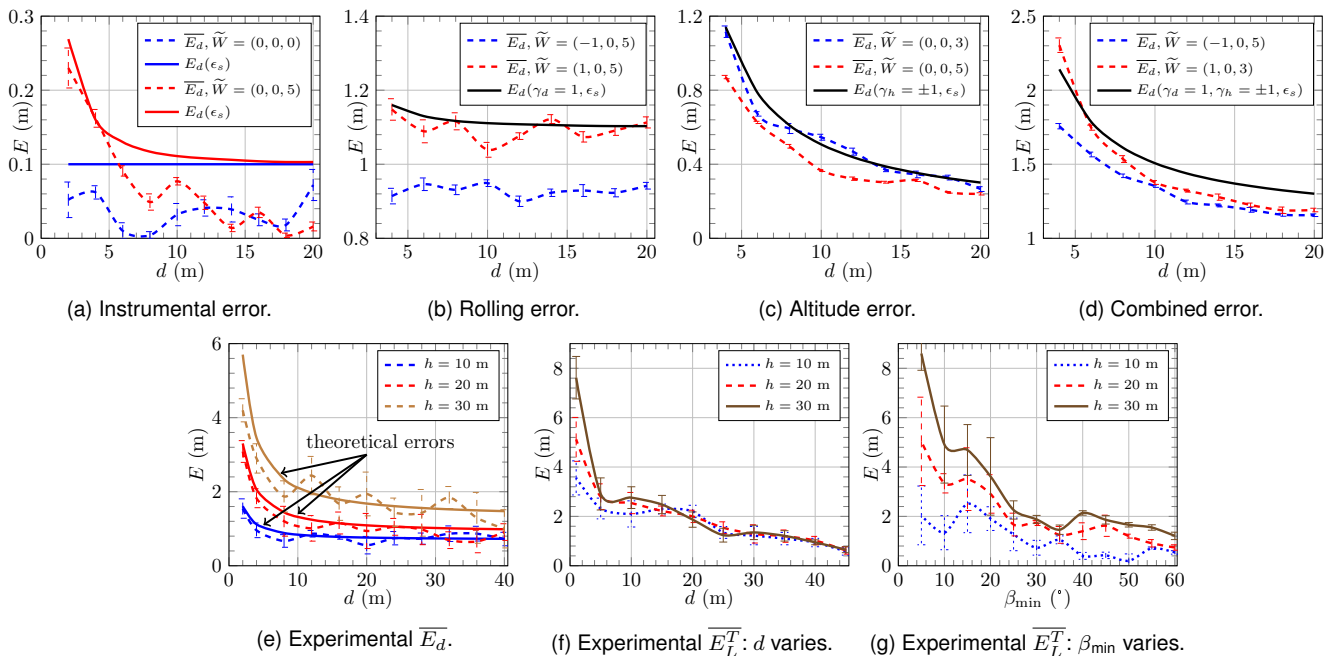


Fig. 9. The experimental error and the theoretical error in different cases.

the GD. In other words, the three points must respect good geometry and minimum distance constraints. In both the experiments we use our 3DR Solo drone as a MA and placed a single GD in $P = (0, 0, 0)$. Moreover, the drone's initial position W' was initially set at the same GD's position, i.e., in $W' = P$.

In the first experiment depicted in Figure 9f, we plot the *experimental localization trilateration error* \overline{E}_L^T between the estimated and the actual position of the GD. Here, we fix the best possible minimum angle $\beta_{\min} = 60^\circ$ and we decrease the value of the ground distance d to smaller values. For each value of d , we perform trilateration using three points which satisfy the optimal geometry. As expected and according to Eq. (8), \overline{E}_L^T is high when d is short, even though the minimum angle is fixed at the best possible value 60° .

In the second experiment shown in Figure 9g we do the opposite by keeping a large and good enough ground distance $d = 40$ m, and decreasing the value of β_{\min} to narrow values. Even here we perform trilateration and according to Eq. (8), the error decreases when β_{\min} increases.

6.4 Comparison of Localization Algorithms

In this section, we describe the hardware and software architecture of the comparative testbed. The goal is to evaluate the performance of different localization algorithms in-field.

In this testbed, we cannot use the previous EVK1000 kit since it is formed by only two antennas, hence it is definitively not sufficient for evaluating a real scenario in which we have to localize multiple GDs at once. Instead, we move towards the larger set of antennas relying on the new MDEK1001 kit from DecaWave, since it comprises of a set of twelve antennas. In addition, the testbed consists also of a Raspberry Pi which is the main component that auto-pilots the drone via Wi-Fi and sends UWB commands via a single UWB antenna that is physically connected to it by the serial peripheral interface (SPI).

6.4.1 Testbed setup

We set a rectangular deployment area of sizes 100×100 m², and fix a Cartesian coordinate system with origin at the special position HOME $(0, 0, h_0 = 1$ m). Then, we deploy on the ground $n = 10$ antennas placed at the top of a tripod of height h_0 . Each antenna (Figure 8c) identified by own ID is not aware of its relative position with respect to the HOME, even though we already know its position. In fact, as illustrated in Figure 10b, the deployed 10 antennas respect a predefined pattern, i.e., form a series of equilateral triangles (shown in green) with the same side of length 30 m in which each vertex is a GD. Thus, we are able to measure, with reasonable accuracy before our experiments, the relative distance between the GDs, with the help of a digital laser. Finally, the HOME position is set between antennas ID 4 and ID 5 accurately measured with the same digital laser.

By a drone's *mission* at a certain altitude h , we actually refer to a drone (see Figure 8d) that flies at a fixed altitude $h_0 + h$ (see Figure 10a) following a certain static path Π . For each algorithm, the trajectory Π starts and finishes at HOME and consists of vertical scans connected by horizontal scans (see Figure 10b). Once all the GDs are deployed, the drone starts its mission flying over the deployment area. When both GD and MA are within the communication range of the other, the devices start a ToA based distance measurement protocol. Then, the GD stores the computed distance along with the current MA's position. In other words, the GD memorizes the position of the waypoint and the associated distance on it. At the end of the mission, each GD estimates its position by invoking a localization algorithm.

All the compared algorithms require at least three points (see Table 3) to compute and estimate the position of a GD. However, each GD has several stored distance measurements, so it can potentially exploit all of them. In order to better understand how either the altitude of the drone or the geometry of the waypoints impact the quality of the

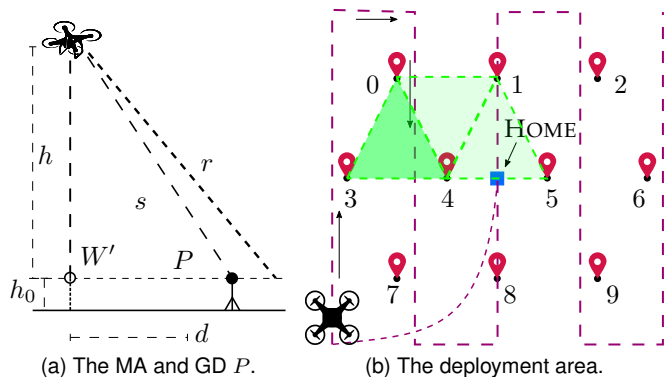


Fig. 10. The experimental testbed on the field.

localization accuracy, as already investigated in Section 6.3, we fix two constraints during the selection of the three points: (i) the ground distance d between the GD and the MA, and (ii) the geometry angle β to keep between the three waypoints. Accordingly, we fix $d = \{20, 30, \dots, 60\}$ m and $\beta = \{0, 15, 30\}^\circ$, where $\beta = 0^\circ$ means an unconstrained geometry. Moreover, we vary the altitude $h = \{10, 20, 30\}$ m. Clearly, it is not easy to find three points at an exact distance d . Thus, we relax the constraint and we search for three points at distance $d \pm \tau$, where τ indicates a tolerance in our measurements (we fix $\tau = 1$ m) due to the fact that the drone sends its position at discrete intervals of time, i.e., the inter-waypoint distance I_w . The I_w value is affected by the drone's speed. In our experiments, we have seen that $I_w = 1$ m with a drone's speed of 10 m/s.

6.4.2 Results

We compare all algorithms varying the drone's altitude h , the minimum distance d among the GDs and the waypoints, and the waypoint geometry. In OMNI, by construction, we select always the furthest three waypoints that guarantee good geometry (see Figure 6a). The OMNI error is reported as a reference for the other algorithms.

In Figure 11, we show the observed errors of SCAN and OMNI along with their theoretical bounds ϵ_L^T given in Eq. (8) obtained by substituting $\epsilon_s = 0.10$ m, and the values of γ_d and γ_h taken from Figure 9e. Obviously, OMNI is better than SCAN because the geometry of the waypoints is enforced. The difference between the theoretical and the observed error is smaller for OMNI than SCAN when $\beta = 0^\circ$, and almost the same when $\beta = 30^\circ$.

Figure 12 compares the localization errors E_L of the algorithms when d varies. The localization error of DRF, IOC, and IOA is greater than that of SCAN and OMNI. As said, the trilateration based algorithms, OMNI and SCAN, get a good localization but pose many constraints (angle, distance) in the selection of waypoints; they also compute the estimated position by performing a least-squares-error optimization technique (which is complex). The DRB-C is not as accurate as OMNI or SCAN because it omits the least-squares-error optimization technique, but it is quite good. The chords based method in DRF is the least accurate. IOC and IOA improve over DRF because their localization technique use the radius information. The errors are large when $\beta = 0^\circ$, while they significantly decrease for all the algorithms when $\beta = 30^\circ$. This shows that all the algorithms,

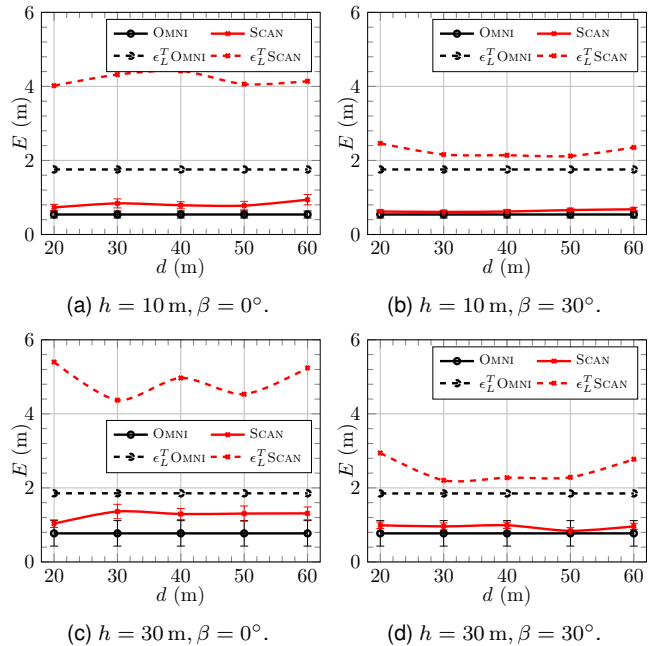


Fig. 11. Errors for SCAN and OMNI.

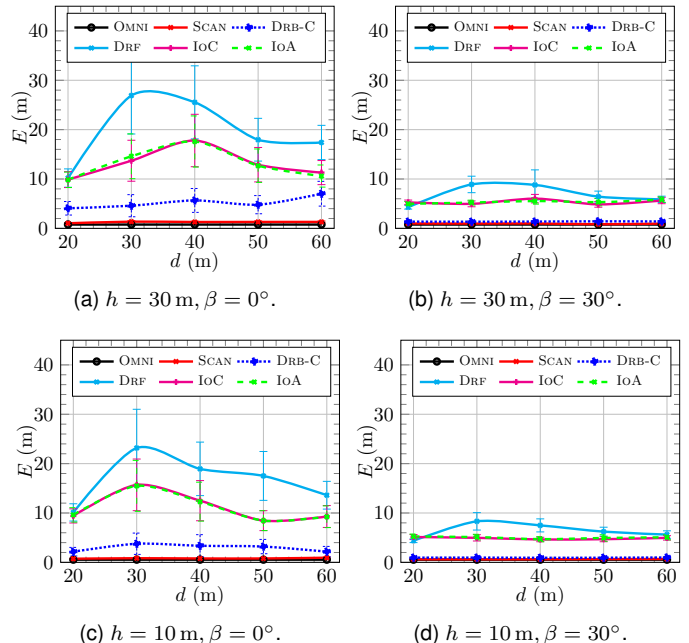


Fig. 12. For fixed h and β , the algorithms error when d varies.

and not only those based on trilateration, benefit from a good waypoint geometry. The experiments with $h = 10$ m in Figures 12c and 12d have a smaller elevation angle and thus a smaller error than those with $h = 30$ m reported in Figures 12a and 12b. When $h = 30$ m, all the ratios yield $h/d \geq 1/3$, and since our experiments are in sub-urban area all the measurements are possibly in LoS; whereas when $h = 10$ m, the measurements at $d \geq 30$ m are mixed LoS and NLoS. Nonetheless, we cannot notice any special behavior, probably, thanks to the UWB multipath immunity.

Figure 13 compares the localization error E_L when $h = 10$ m and $d = 30$ m or $d = 50$ m, varying the geometry angle β . From the observed errors, any localization that satisfies $\beta \geq 30^\circ$ has a small error, and cannot significantly improve decreasing the elevation angle (i.e., ratio h/d). The decrease

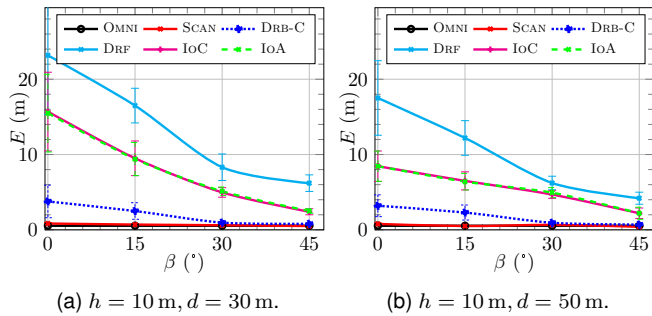


Fig. 13. For fixed h and d , the algorithms error when β varies.

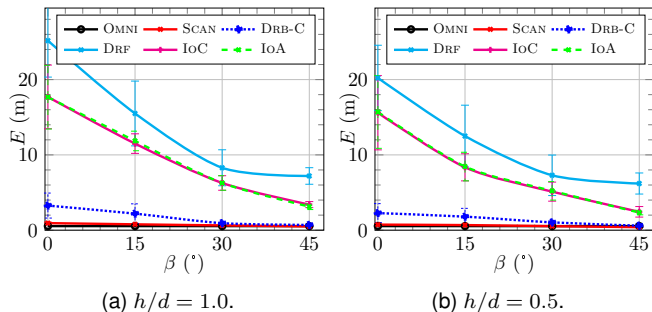


Fig. 14. For fixed h/d ratio, the algorithms error when β varies.

of the error when h decreases from 50 m to 30 m is large when $0^\circ \leq \beta \leq 30^\circ$. Finally, note that in Figure 13b, it holds $h/d = 0.2$, which is below the ratio that guarantees 100% LoS in sub-urban area in Table 2, but we do not notice a meaningful worsening of the error.

Figure 14 plots the error for different pairs of h and d with the same ratio h/d . Precisely, we compare two ratios h/d : 0.5 and 1.0. Each ratio can be extracted from three different combinations altitude/distance. For example, for $h/d = 0.5$ we consider the combinations $h = \{10, 20, 30\}$ m and $d = \{20, 40, 60\}$ m. The improvement in the accuracy is high when the elevation angle decreases from 45° to 26° . DRF, the least accurate algorithm in all our experiments, is very sensitive to the change of the elevation angle.

TABLE 4

Error between range-free and range-based algorithms, in meters (m).

	DRF		IoC		IoA	
	RF	RB	RF	RB	RF	RB
	h (m)					
10	52.3	16.6	48.8	10.8	47.2	10.8
20	55.1	19.8	49.1	11.2	48.8	11.0
30	57.7	20.4	48.2	13.8	51.2	13.6

In conclusion, in Table 4 compares the localization error E_L among range-free (RF) and range-based (RB) versions of the three original range-free algorithms DRF, IoC, and IoA, for different altitudes h . In particular, we report the localization error obtained from our previous testbed [15] on which the three algorithms were implemented as pure range-free techniques based on the HnH technique (RF columns), along with the average results shown in Figure 12 (RB columns). As reported in [15], on average, the experimental error of those algorithms is very large (almost 60 m) and variable. These experiments show that the error of the original range-free versions is 3-4 times larger than the corresponding extended range-based version that exploit distance measurements. Moreover, in [15], about one-third

of the GDs were left unlocalized by IoC and IoA, while DRF localized all of them. These results and the fact that our antennas are able to take distance measurements via ToA fully justify our transformation of DRF, IoC, and IoA in range-based algorithms, implying that measurements help.

7 CONCLUSIONS

In this paper, we analytically study and experimentally evaluate through real experiments on the field the errors that can affect the localization of GDs using a drone as MA. We decompose the error in measurement error, ground error, and localization error, and provide analytical expressions of these errors. We also link the ground error with the theory of the A2G communication link via the elevation angle. Our experiments confirm that our analytical analysis is accurate. Furthermore, results also show that extending range-free algorithms with range-based measurements, significantly increases the localization accuracy.

In the future, we plan to extend the analysis to NLoS scenarios. We will investigate DecaWave antenna capabilities, and also modulating and tuning the transmitting power in different scenarios. We finally plan to extend our work to propose a more realistic antenna radiation pattern.

Acknowledgments: The authors are grateful to the editor and reviewers for valuable comments that helped us improve the quality of the manuscript. This work was partially supported by Project *NALP-SAPR* granted by FSE, Project *NALP-SAPR2* granted by University of Perugia, by NATO grant G4936, Intelligent Systems Center (ISC) at Missouri S&T, and by NSF grants CNS-1545050, CNS-1725755, CNS-1818942, and SCC-1952045.

REFERENCES

- [1] N. H. Motlagh, T. Taleb, and O. Arouk, "Low-altitude unmanned aerial vehicles-based internet of things services: Comprehensive survey and future perspectives," *IEEE Internet of Things Journal*, vol. 3, no. 6, pp. 899–922, 2016.
- [2] S.-S. Choi and E.-K. Kim, "Building crack inspection using small UAV," in *17th International IEEE Conference on Advanced Communication Technology (ICACT)*, 2015, pp. 235–238.
- [3] N. Gao, J. Zhao, D. Song, J. Chu, K. Cao, X. Zha, and X. Du, "High-precision and light-small oblique photogrammetry uav landscape restoration monitoring," in *2018 9th International Conference on Intelligent Control Information Processing*. IEEE, 2018, pp. 301–304.
- [4] D. Kang and Y.-J. Cha, "Autonomous uavs for structural health monitoring using deep learning and an ultrasonic beacon system with geo-tagging," *Computer-Aided Civil and Infrastructure Engineering*, vol. 33, no. 10, pp. 885–902, 2018.
- [5] D. C. Tsouros, A. Triantafyllou, S. Bibi, and P. G. Sarigannidis, "Data acquisition and analysis methods in uav-based applications for precision agriculture," in *2019 15th International Conference on Distributed Computing Sensor Systems*. IEEE, 2019, pp. 377–384.
- [6] M. Silvagni, A. Tonoli, E. Zenerino, and M. Chiaberge, "Multipurpose uav for search and rescue operations in mountain avalanche events," *Geomatics, Natural Hazards and Risk*, vol. 8, no. 1, pp. 18–33, 2017.
- [7] N. B. Priyantha, H. Balakrishnan, E. D. Demaine, and S. J. Teller, "Anchor-free distributed localization in sensor networks." in *Sensys*, vol. 3, 2003, pp. 340–341.
- [8] G. Han, J. Jiang, C. Zhang, T. Q. Duong, M. Guizani, and G. K. Karagiannidis, "A survey on mobile anchor node assisted localization in wireless sensor networks," *IEEE Communications Surveys & Tutorials*, vol. 18, no. 3, pp. 2220–2243, 2016.
- [9] A. Malhotra and S. Kaur, "A comprehensive review on recent advancements in routing protocols for flying ad hoc networks," *Transactions on Emerging Telecommunications Technologies*, p. e3688, 2019.

- [10] I. Bekmezci, O. K. Sahingoz, and S. Temel, "Flying ad-hoc networks (fanets): A survey," *Ad Hoc Networks*, vol. 11, no. 3, pp. 1254–1270, 2013.
- [11] M. W. Mueller, M. Hamer, and R. D'Andrea, "Fusing ultra-wideband range measurements with accelerometers and rate gyroscopes for quadcopter state estimation," in *2015 International Conference on Robotics Automation*. IEEE, 2015, pp. 1730–1736.
- [12] K.-F. Ssu, C.-H. Ou, and H. C. Jiau, "Localization with mobile anchor points in wireless sensor networks," *IEEE transactions on Vehicular Technology*, vol. 54, no. 3, pp. 1187–1197, 2005.
- [13] B. Xiao, H. Chen, and S. Zhou, "Distributed localization using a moving beacon in wireless sensor networks," *IEEE Transactions on Parallel and Distributed Systems*, vol. 19, no. 5, pp. 587–600, 2008.
- [14] F. B. Sorbelli and C. M. Pinotti, "Ground localization with a drone and uwb antennas: Experiments on the field," in *2019 IEEE 20th International Symposium on "A World of Wireless, Mobile and Multimedia Networks" (WoWMoM)*. IEEE, 2019, pp. 1–7.
- [15] F. B. Sorbelli, C. M. Pinotti, and G. Rigoni, "Range-free localization algorithms with mobile anchors at different altitudes: A comparative study," in *Proceedings of the 21st International Conference on Distributed Computing and Networking*, 2020, pp. 1–10.
- [16] M. Laaraiedh, L. Yu, S. Avrillon, and B. Uguen, "Comparison of hybrid localization schemes using rssi, toa, and tdoa," in *17th European Wireless 2011-Sustainable Wireless Technologies*. VDE, 2011, pp. 1–5.
- [17] DecaWave, *DecaWave Ltd: EVK1000 Evaluation Kit*, 2019, <https://www.decawave.com/product/evk1000-evaluation-kit/>.
- [18] GPS.gov, *GPS Accuracy*, 2020, <https://www.gps.gov/systems/gps/performance/accuracy/>.
- [19] 3D Robotics, *Solo Specs: Solving commonly found errors for copters*, 2019, https://3dr.com/support/articles/troubleshooting_guide/.
- [20] F. Thomas and L. Ros, "Revisiting trilateration for robot localization," *IEEE Transactions on robotics*, vol. 21, no. 1, pp. 93–101, 2005.
- [21] J. Blumenthal, R. Grossmann, F. Golatowski, and D. Timmermann, "Weighted centroid localization in zigbee-based sensor networks," in *2007 IEEE international symposium on intelligent signal processing*. IEEE, 2007, pp. 1–6.
- [22] N. Bulusu, J. Heidemann, D. Estrin *et al.*, "Gps-less low-cost outdoor localization for very small devices," *IEEE personal communications*, vol. 7, no. 5, pp. 28–34, 2000.
- [23] F. B. Sorbelli, C. M. Pinotti, and V. Ravelomanana, "Range-free localization algorithm using a customary drone: Towards a realistic scenario," *Pervasive and Mobile Computing*, vol. 54, pp. 1–15, 2019.
- [24] S. Lee, E. Kim, C. Kim, and K. Kim, "Localization with a mobile beacon based on geometric constraints in wireless sensor networks," *IEEE Transactions on Wireless Communications*, vol. 8, no. 12, pp. 5801–5805, 2009.
- [25] F. B. Sorbelli, S. K. Das, C. M. Pinotti, and S. Silvestri, "Range based algorithms for precise localization of terrestrial objects using a drone," *Pervasive and Mobile Computing*, vol. 48, pp. 20–42, 2018.
- [26] D. Koutsonikolas, S. M. Das, and Y. C. Hu, "Path planning of mobile landmarks for localization in wireless sensor networks," *Computer Communications*, vol. 30, no. 13, pp. 2577–2592, 2007.
- [27] DecaWave, *MDEK1001 Development Kit*, 2019, <https://www.decawave.com/product/mdek1001-deployment-kit/>.
- [28] J. Jiang, G. Han, H. Xu, L. Shu, and M. Guizani, "Lmat: Localization with a mobile anchor node based on trilateration in wireless sensor networks," in *Global Telecommunications Conference (GLOBECOM 2011)*, 2011 IEEE. IEEE, 2011, pp. 1–6.
- [29] P. Perazzo, F. Betti Sorbelli, M. Conti, G. Dini, and C. M. Pinotti, "Drone Path Planning for Secure Positioning and Secure Position Verification," *IEEE Transactions on Mobile Computing*, vol. 16, no. 9, pp. 2478–2493, 2017.
- [30] D. Ebrahimi, S. Sharafeddine, P.-H. Ho, and C. Assi, "Autonomous uav trajectory for localizing ground objects: A reinforcement learning approach," *IEEE Transactions on Mobile Computing*, 2020.
- [31] G. Greco, C. Lucianaz, S. Bertoldo, and M. Allegretti, "Localization of rfid tags for environmental monitoring using uav," in *Research and Technologies for Society and Industry Leveraging a better tomorrow*, 2015 IEEE 1st International Forum on. IEEE, 2015, pp. 480–483.
- [32] J. Grigulo and L. B. Becker, "Experimenting sensor nodes localization in wsn with uav acting as mobile agent," in *2018 IEEE 23rd International Conference on Emerging Technologies and Factory Automation (ETFA)*, vol. 1. IEEE, 2018, pp. 808–815.
- [33] K. Cisek, A. Zolich, K. Klausen, and T. A. J., "Ultra-wide band real time location systems: Practical implementation and uav performance evaluation," in *2017 Workshop on Research, Education, Development of Unmanned Aerial Systems*. IEEE, 2017, pp. 204–209.
- [34] F. Lazzari, A. Buffi, P. Nepa, and S. Lazzari, "Numerical investigation of an uwb localization technique for unmanned aerial vehicles in outdoor scenarios," *IEEE Sensors Journal*, vol. 17, no. 9, pp. 2896–2903, 2017.
- [35] A. Al-Hourani, S. Kandeepan, and S. Lardner, "Optimal lap altitude for maximum coverage," *IEEE Wireless Communications Letters*, vol. 3, no. 6, pp. 569–572, 2014.
- [36] DecaWave, *Narrowband versus Ultra-Wideband*, 2019, <http://site.ieee.org/com-rc/files/2017/09/DecaWaveANLN2013.pdf>.
- [37] F. Betti S., S. K. Das, C. M. Pinotti, and S. Silvestri, "On the accuracy of localizing terrestrial objects using drones," in *International Conference Communications (ICC)*. IEEE, 2018, pp. 1–7.
- [38] Bosch, *Laser Measuring*, 2020, <https://www.boschtools.com/us/en/boschtools-ocs/laser-measuring-glm400c-197704-p/>.



Francesco Betti Sorbelli received the Bachelor and Master degrees *cum laude* in Computer Science from the University of Perugia, Italy, in 2007 and 2010, respectively, and his Ph.D. in Computer Science from the University of Florence, Italy, in 2018. After his Ph.D., he was a Postdoc Researcher at University of Perugia. Currently, he is a Postdoc at the Missouri University of Science and Technology University, USA. His research interests include wireless sensor networks, algorithms on drones and robots.



Cristina M. Pinotti received the Master degree *cum laude* in Computer Science from the University of Pisa, Italy, in 1986. In 1987-1999, she was Researcher with the National Council of Research in Pisa. In 2000-2003, she was Associate Professor at the University of Trento. Since 2004, she is a Full Professor at the University of Perugia. Her current research interests include the design and analysis of algorithms for wireless sensor networks and communication networks. She has published more than 100 refereed papers on international journals and conferences, workshops, and book chapters.



Simone Silvestri graduated with honors and received his PhD in computer science at Sapienza University of Rome, Italy. He is an Assistant Professor in the Department of Computer Science of the University of Kentucky. His research interests include cyber-physical-human systems, Internet of Things, hybrid sensor networks, and network management. He serves as Associate Editor of Elsevier's *Pervasive and Mobile Computing* journal, and has served on the Technical Program Committees of numerous international conferences. His research is funded by several agencies such as NIFA, NSF, and NATO. He received the NSF CAREER award in 2020.



Sajal K. Das is a professor of computer science and Daniel St. Clair Endowed Chair at Missouri University of Science and Technology. His research interests include wireless sensor networks, mobile and pervasive computing, cyber-physical systems and IoT, smart environments, cloud computing, cyber security, and social networks. He serves as the founding Editor-in-Chief of Elsevier's *Pervasive and Mobile Computing* journal, and as Associate Editor of several journals including the *IEEE Transactions of Mobile Computing*, *IEEE Transactions on Dependable and Secure Computing*, and *ACM Transactions on Sensor Networks*. He is an IEEE Fellow.